ORIGINAL ARTICLE

A metabolic intervention strategy to break evolutionary adaptability of tumor for reinforced immunotherapy

Qianhua Feng[a,b], Yutong Hao[a], Shuaiqi Yang[a], Xiaomin Yuan[a], Jing Chen[a], Yuying Mei[a], Lanlan Liu[d], Junbiao Chang[b,c,*], Zhenzhong Zhang[a,b,*], Lei Wang[a,b,*]

[a]School of Pharmaceutical Sciences, Zhengzhou University, Zhengzhou 450001, China
[b]Henan Key Laboratory of Targeting Therapy and Diagnosis for Critical Diseases, Zhengzhou 450001, China
[c]College of Chemistry, Zhengzhou University, Zhengzhou 450001, China
[d]Department of Pharmacy, The Third Affiliated Hospital of Zhengzhou University, Zhengzhou 450052, China

Abstract The typical hallmark of tumor evolution is metabolic dysregulation. In addition to secreting immunoregulatory metabolites, tumor cells and various immune cells display different metabolic pathways and plasticity. Harnessing the metabolic differences to reduce the tumor and immunosuppressive cells while enhancing the activity of positive immunoregulatory cells is a promising strategy. We develop a nanoplatform (CLCeMOF) based on cerium metal−organic framework (CeMOF) by lactate oxidase (LOX) modification and glutaminase inhibitor (CB839) loading. The cascade catalytic reactions induced by CLCeMOF generate reactive oxygen species "storm" to elicit immune responses. Meanwhile, LOX-mediated metabolite lactate exhaustion relieves the immunosuppressive tumor microenvironment, preparing the ground for intracellular regulation. Most noticeably, the immunometabolic checkpoint blockade therapy, as a result of glutamine antagonism, is exploited for overall cell mobilization. It is found that CLCeMOF inhibited glutamine metabolism-dependent cells (tumor cells, immunosuppressive cells, etc.), increased infiltration of dendritic cells, and especially reprogrammed CD8$^+$ T lymphocytes with considerable metabolic flexibility toward a highly activated, long-lived, and memory-like phenotype. Such an idea intervenes both metabolite (lactate) and cellular metabolic pathway, which essentially alters

overall cell fates toward the desired situation. Collectively, the metabolic intervention strategy is bound to break the evolutionary adaptability of tumors for reinforced immunotherapy.

1. Introduction

In recent years, tumor evolution has been considered a cumulative intrinsic process with metabolic dysregulation[1]. Both immunosuppressive metabolites and cellular metabolic pathways contribute to tumor progression and impaired antitumor immunity[2−4]. Considering that the metabolism plays a crucial role in cell viability and differentiation, the metabolic intervention is a promising strategy to reprogram the immune state prior to the evolutionary adaption of tumor for reinforced immunotherapy, and the resulting overall cells mobilization of which is more meaningful compared with the single immune cell modulation in most reports[5−9].

More evidence shows that some tumor metabolites with immunoregulatory function control the autoimmunity[10]. For example, lactate, the waste product of glycolysis is responsive for immunosupppressive tumor microenvironment (TME), inducing immune escape of tumor cells[11,12]. Thus, lactate exhaustion is a good idea to reprogram TME toward a friendly environment for reinforced immunotherapy[13−15]. Lactate oxidase (LOX) can catalyze the oxidation of lactate to pyruvate and H_2O_2, which is an efficient and direct way to deplete lactate, however, it is rarely reported due to poor stability[16,17]. Fortunately, cerium-based metal−organic framework (CeMOF) with high porosity and large surface area can be employed as a carrier for LOX immobilization[18−20]. Furthermore, CeMOF with oxidase-like activity converts H_2O_2 (the by-product of lactate oxidation) into hydroxyl radicals ($\cdot$OH) in acidic TME[21,22]. Therefore, such lactate targeted metabolite intervention contributes to the TME reprogramming, as well as the nanocytalytic reactions for reactive oxygen species (ROS) mediated immunogenic tumor cell death (ICD) (Fig. 1)[22-25]

Although the TME regulation is promising, the specific cellular metabolism modulation merits serious consideration. It is reported that the metabolic pathways and plasticity differ among tumor cells and various immune cells[26−28]. Thus, harnessing metabolic differences to intervene in a certain metabolic pathway should reprogram various cells. Of several metabolic pathways, glutamine metabolism is significant for the tricarboxylic acid cycle, and antagonism of which can be exploited for "immuno-metabolic checkpoint" blockade therapy[29−31]. Interestingly, CB839 as a glutaminase inhibitor cut off glutamine metabolism, showing admirable therapeutic effects in phase I clinical trials. The CB839-loaded nanoplatform in this work was found to inhibit glutamine metabolism-dependent immunosuppressive cells such as regulatory T cells (Tregs), myeloid-derived suppressor cells (MDSCs), and M2 tumor-associated macrophages (TAMs). Conversely, through upregulating acetate metabolism instead, $CD8^+$ T lymphocytes with considerable metabolic flexibility were reprogrammed toward a $CD8^+$ T_{high} (highly activated, long-lived and memory-like) phenotype[32]. Additionally, considering glutathione (GSH) is known as the reactive oxygen species (ROS) scavenger that sulfhydryl groups in GSH are easily oxidized by

ROS[33,34], CB839 can indirectly enhance ROS "storm" in LOX-CeMOF catalytic system through metabolically reducing GSH generation.

Taking advantage of the metabolic properties of the tumor, we proposed to intervene in both lactate and glutamine metabolism to reprogram TME as well as the metabolism of various cells (Fig. 1). Briefly, a nanoplatform based on CeMOF by LOX modification and CB839 loading was constructed. The cascade catalytic reactions among LOX, CeMOF and CB839 brought out ROS "storm", further eliciting immune responses. On the one hand, lactate exhaustion repolarized the immunosuppressive microenvironment toward one supporting antitumor immunity, which prepared the ground for intracellular regulation. On the other hand, the glutamine antagonism-induced metabolic checkpoint blockade therapy mobilized overall cells. The CLCeMOF was found to replolarize TAMs and increased the infiltration of dendritic cells (DCs). And the reprogramming $CD8^+$ T_{high} lymphocytes were responsible for potent antitumor responses. Utilizing a metabolic intervention strategy, the nanoplatform (CLCeMOF) essentially altered overall cell fates toward the desired situation, which reinforced immunotherapy and prevented tumor development prior to the evolutionary adaption of the tumor.

2. Materials and methods

2.1. Materials

Lactate oxidase (LOX), N-(3-dimethylamino propyl-N'-ethyl-carbodiimide) hydrochloride (EDC·HCl) and N-hydroxysuccinimide (NHS) were purchased from Shanghai Macklin Biochemical Co., Ltd. (Shanghai, China). CB839 was brought from APExBIO (Houston, TX, USA). Moreover, FITC-anti-CD86, PE-anti-CD206, APC-anti-CD40, APC-Cy7-anti-CD45, BV510-anti-CD3, FITC-anti-CD4, PE-anti-CD8, BV421-anti-F4/80, FITC-anti-CD11b, PE-anti-CD86, APC-anti-CD206, BV605-anti-Ly-6G, PE-Cy7-anti-Ly-6C, antibodies were supplied by BD Biosciences (San Jose, CA, USA). Other reagents were standard Sinopharm Chemical Reagent (Shanghai, China).

2.2. Synthesis of CLCeMOF

Terephthalic acid and $Ce(NH_4)_2(NO_3)_6$ were dissolved in dimethylformamide and then received oil bath at 100 °C for 15 min. The obtained white precipitate was calcined under nitrogen protection at 400 °C for 5 h to produce CeMOF. To introduce LOX onto the surface of CeMOF, LOX in PBS was activated by EDC·HCl and NHS for 0.5 h. Then CeMOF was added into the mixture and stirred for 24 h. The resultant LCeMOF was washed and concentrated. For CB839 loading, LCeMOF and CB839 (1:1 w/w) were dissolved in ethanol−water mixture (ethanol:water = 1:1). After stirring for 24 h, CLCeMOF was collected by centrifugation. Free CB839 in supernatants was collected and quantified spectrophotometrically at
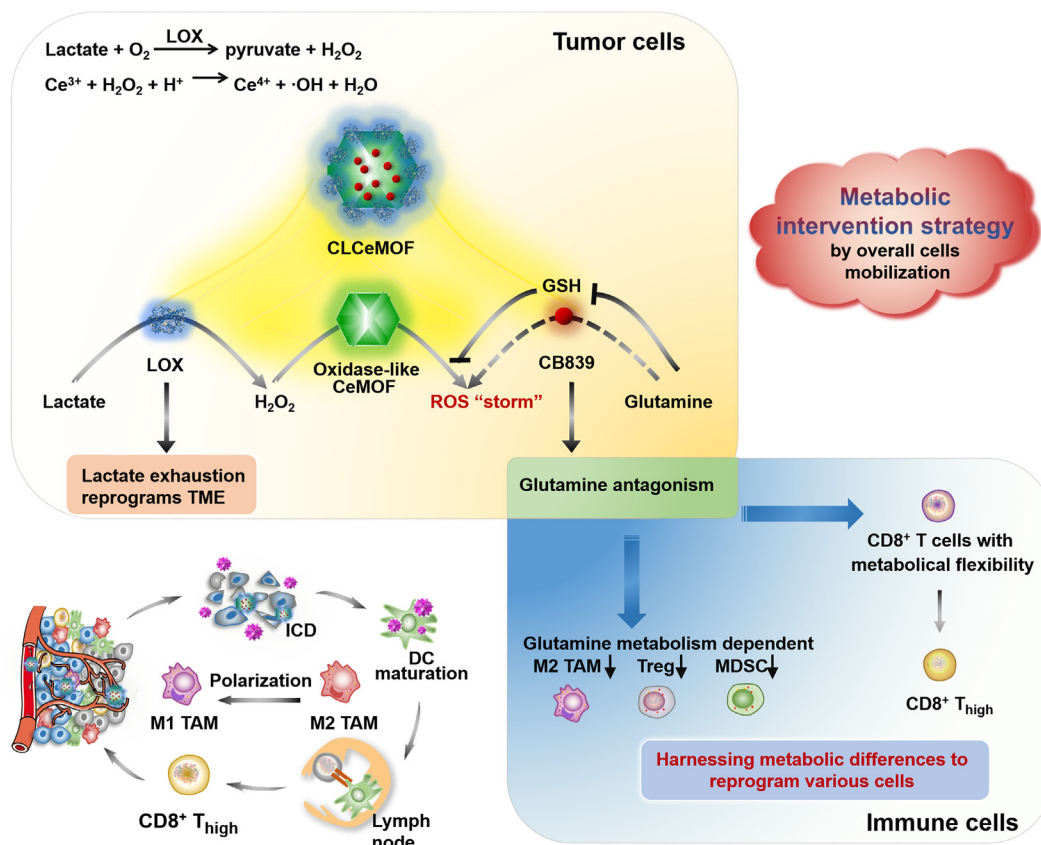
Figure 1 Schematic mechanism of CLCeMOF to break evolutionary adaptability of the tumor. Metabolically intervention strategy herein reinforced immunotherapy by general tumoral cells mobilization.

243 nm. CB839 loading efficiency was calculated according to the following Eqs. (1) and (2):

$$Mass_{CB839\text{-}loaded} = Mass_{CB839\text{-}prep} - Mass_{CB839\text{-}free} \tag{1}$$

$$CB839 \text{ loading efficiency} = Mass_{CB839\text{-}loaded} \, / \, (Mass_{CB839\text{-}loaded} + Mass_{LCeMOF}) \tag{2}$$

2.3. Characterization of CLCeMOF

Transmission electron microscopy (TEM, model JEOL-2000, JEOL, Tokyo, Japan) was used to observe the morphology of the sample. The valence distribution of elements in CeMOF was recorded using X-ray photoelectron spectroscopy (XPS, ESCA-750, Shimadzu, Kyoto, Japan). FT-IR spectra were obtained by using an FT-IR spectrometer (Vertex 70, Bruker Optics Inc., Billerica, MA, USA). X-ray diffractometer (XRD, X'Pert PRO, PANalytical, Almelo, Netherlands) was used to detect the crystallographic structure of the sample. The amount of LOX in LCeMOF was measured by a thermogravimetric analyzer (TGA-50H, Shimadzu, Kyoto, Japan), as well as BCA protein assay. A drug release experiment was conducted in PBS with the dialysis method.

2.4. Detection of lactate consumption

CeMOF, LOX and LCeMOF were incubated with lactate for 24 h, respectively. Then the residue of lactate was detected by lactate assay kit.

2.5. Hydroxyl radicals generation detection

ABTS could react with $\cdot$OH to generate ABTS$^{+\cdot}$ with a characteristic absorption peak at 418 nm. Based on this, CeMOF with different concentrations was incubated with H_2O_2 as well as ABTS at pH 6 at different times. Then UV spectra of the supernatants were recorded. What's more, CeMOF and LCeMOF were incubated with different lactate as well as ABTS to investigate the cascade catalytic ability.

2.6. Intracellular ROS detection

4T1 mouse breast cancer cells were treated with PBS, CeMOF, LCeMOF and CLCeMOF for 6 h in medium-containing lactate, respectively, and then were further incubated with DCFH-DA probe. Then cells were analyzed by confocal laser scanning microscope (CLSM, Leica TCS SP8, Germany).

2.7. Cell cytotoxicity

4T1 cells were incubated with different formulations (CeMOF: 50 µg/mL, LOX: 0.03 µg/mL, CB839: 3 µmol/L) and lactate (0, 2, 5 mmol/L) for 24 h. At last, cell viability was measured by using MTT assay.

2.8. Immune response in vitro

4T1 cells were incubated with formulations in medium-containing lactate. 6 h later, cells were stained with Alexa Fluor 488-CRT

antibody for CLSM imaging (Leica), the cell supernatant was examined by using HMGB1 detection kit. Additionally, a transwell system was carried out to assess the DCs maturation behavior. 4T1 cells and DCs were seeded in the upper and lower compartments, respectively. After different treatments, DCs maturation was conducted for flow cytometry analysis (BD Accuri C6, Becton Dickinson, Franklin Lakes, NJ, USA). For TAMs polarization measurement, bone marrow-derived macrophages were cultured with LPS or IL-4 to generate M1-TAM or M2-TAM, respectively. TAM was treated with formulations and then stained with anti-CD86-FITC and anti-CD206-PE. After that, cells were analyzed by flow cytometry (BD Accuri C6). What's more, cell supernatant was collected for IL-12 and IL-10 detection by ELISA.

2.9. Animal model

Animal experiments were approved by the Committee for Experimental Animals Welfare and Ethics of Zhengzhou University (Zhengzhou, China). Femal BALB/c mice were purchased form Zhengzhou Huaxing Experimental Animal Farm (China). 4T1 tumor-bearing mice were built by subcutaneous injection with 4T1 cells (100 μL, 10^7 cells/mL) on the right flank of mice.

2.10. In vivo antitumor activity

4T1 tumor-bearing mice were divided into 6 groups. Mice were i.v. injected with saline, CeMOF, CB839, LCeMOF and CLCeMOF ([CB839] = 2.1 mg/kg [CeMOF] = 6 mg/kg) every 2 days for 7 times. Tumors volume and body weights were measured. On Day 35, tumors were removed for hematoxylin and eosin (H&E), TUNEL staining. And tumors were homogenized, followed by centrifuging. The glutaminase and lactate levels in the supernatant were detected by using Western blotting techniques and lactate assay kit, respectively. In addition, the survival rate of mice was monitored for 50 days similarly by antitumor activity method.

2.11. The tumor recurrence prevention experiment

4T1 tumor-bearing mice were injected with a formulation similarly to antitumor activity method. After treatment for 14 days, the tumor residues were surgically removed 7 days post the final treatment. Twenty-one days later, mice were rechallenged with i.v. injection of 4T1-luc cells to establish the tumor relapse mouse model. Finally, lungs were harvested and taken for H&E staining. The metastasis nodules were counted and analyzed.

2.12. Antitumor immunity evaluation

4T1 tumor-bearing mice were i.v. administered formulation at the abovementioned doses. On Day 7, mice were sacrificed, and cytokine secretion in serum was detected by ELISA. Tumors were removed for CRT, FoxP3^{+}, Gr-1^{+}, CD4^{+}, CD8^{+}, Arg-1, TNF-α and iNOS staining, respectively. The CD69 and MCL-1 protein on CD8^{+} T lymphocytes were also stained to investigate the cell function. In addition, population of infiltrating lymphocytes in tumors and lymph nodes was detected by flow cytometry assay (BD Accuri C6).

2.13. Metabolic and transcriptomic analysis

4T1 tumor-bearing mice were i.v. injected with saline and CLCe-MOF ([CB839] = 2.1 mg/kg [CeMOF] = 6 mg/kg) for 14 days,

respectively. Mice were sacrificed, tumors were removed and the high-throughput sequencing was conducted in Wuhan Servicebio Technology Co., Ltd (Wuhan, China). The data were analyzed online with I-Sanger Cloud Platform. Functional association networks of the immune-related genes were obtained on the website of STRING (https://string-db.org/). In addition, metabolic analysis based on UPLC−MS/MS was also carried out. Metabolomic small molecule compound rapid identification and analysis software (OSI-SMMS) was used to analyze small molecule metabolites. SIMCA-P software (version 13.0, Umetrics, Umea, Sweden) was conducted for data analyses and modeling. The screened differential compounds were analyzed on MetaboAnalyst official website (http://www.metaboanalyst.ca/) for the relevant metabolic pathways associated with these differential compounds.

2.14. Statistical analysis

Results were expressed as mean ± standard deviation (SD) from at least three independent measurements. All data sets were analyzed by using GraphPad Prism6 software and identified by one-way ANOVA. The level of significance was set at probabilities of $^*P < 0.05$, $^{**}P < 0.01$ and $^{***}P < 0.001$.

3. Results and discussion

3.1. Synthesis and characterizations of CLCeMOF

The TEM image of CeMOF showed its irregular structure with a particle size of ∼150 nm, and the ultra-small CeO_2 particles with 5 nm were evenly arranged on the MOFs frame (Fig. 2B). Both HAADF-STEM-based elemental mapping and EDS pattern further confirmed the distribution of three elements (Ce, C and O) on CeMOF (Fig. 2B and Supporting Information Fig. S1). The XRD peaks of CeMOF appeared at the positions of 28.8°, 33.3°, 47.6° and 56.4° corresponded, respectively to (111) (200), (220), and (311) crystal planes (Supporting Information Fig. S2), which indicated their cubic fluorite structure (JCPDF no. 34-0394). Next, LOX was introduced onto the surface of CeMOF via an amidation reaction. FT-IR results with a new −NH−CO− stretching vibration at 1654 cm^{-1} in Fig. 2D confirmed the successful LOX immobilization. What's more, the TEM of LOX-CeMOF (LCe-MOF) showed a smooth edge and exhibited a thin film-like layer of LOX on the surface of CeMOF (Fig. 2C). The amount of LOX in LCeMOF was measured as 13.2% according to BCA protein assay. N_2 adsorption−desorption isotherm of CeMOF exhibited a type IV isothermal curve with a specific surface area of 70.7 m^2/g and an average pore diameter of 8.3 nm (Supporting Information Fig. S3), providing a venue for drug loading. And the loading efficiency of CB839 in CLCeMOF was 7.2%, the dose of which was sufficient for high therapeutic efficacy. The drug release profile of CLCeMOF at different pH values was explored (Fig. 2E). It showed that the CLCeMOF as the drug delivery system exhibited a sustained-release pattern in comparison with the free CB839 group. Notably, CB839 release from CLCeMOF increased by about 38.5% at pH 5.5 than that at pH 7.4, indicating an acidic pH-responsive drug release profile of the nanoplatform due to the protonation of amino group on CB839. On the basis of the acidic tumor microenvironment, it was plausible to infer that CLCeMOF should plenarily exert its therapeutic efficacy at the tumor site and open up new possibilities for a more sophisticated on-demand cargo delivery.
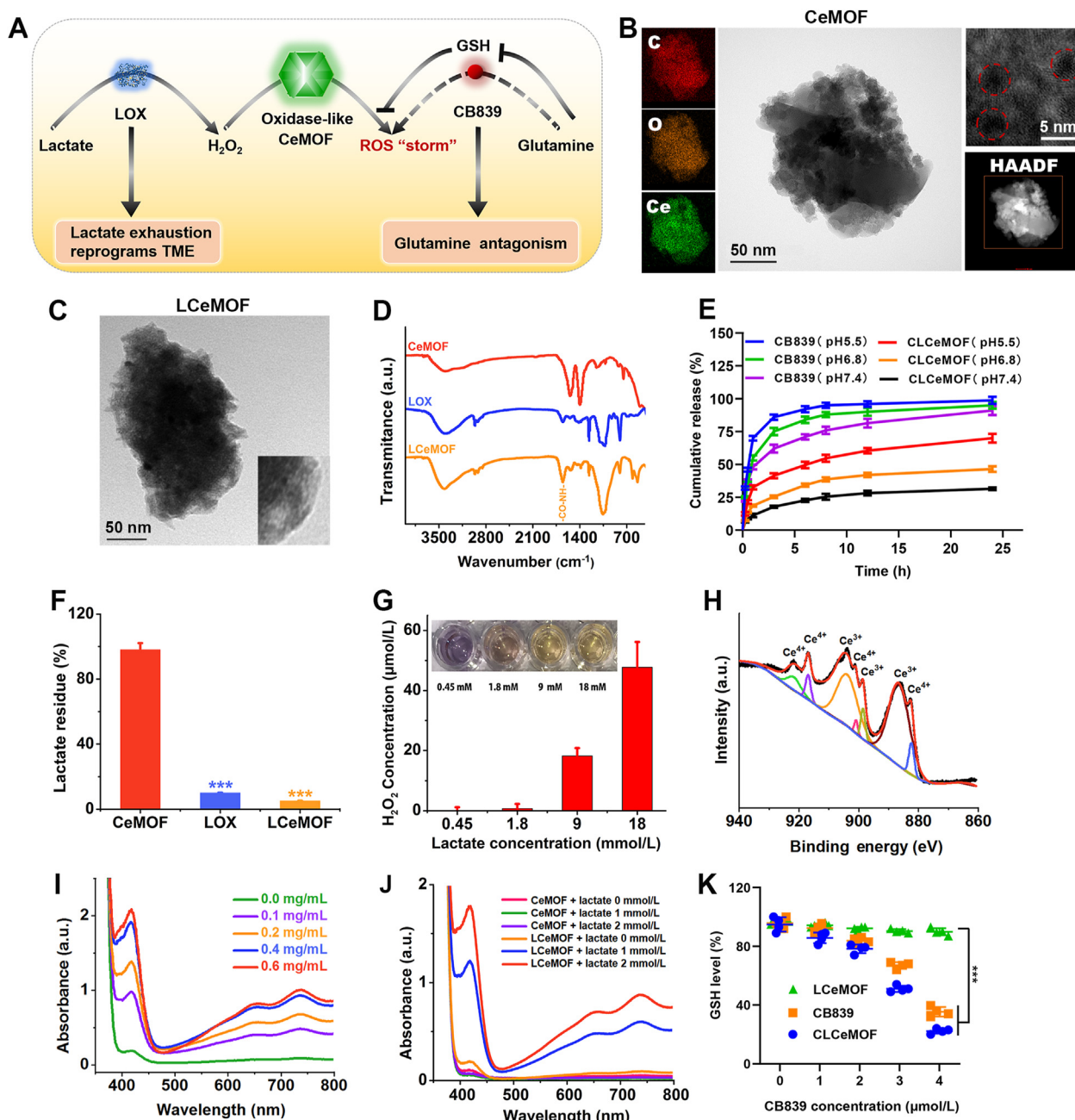
Figure 2 Characterizations of CLCeMOF. (A) Schematic picture of cascade catalytic reactions in CLCeMOF to bring out "ROS" storm (B) TEM image of CeMOF. The ultra-small CeO_2 particles were evenly arranged on the MOFs frame. (C) TEM of LCeMOF (D) FT-IR spectra. (E) The drug release profile of CB839 and CLCeMOF in PBS ($n = 3$). (F) Lactate consumption after different treatments ($n = 3$). ***$P < 0.001$ *versus* CeMOF group. (G) H_2O_2 generation detection after incubating lactate with LOX ($n = 3$). (H) XPS spectrum of CeMOF (I) ·OH generation followed by oxidization reaction of ABTS into ABTS$^{·+}$. CeMOF with different concentrations was incubated with H_2O_2 at pH 6 for 10 min. (J) ·OH generation detection after different treatments (K) GSH level detection in 4T1 cells ($n = 4$). Data are presented as mean $\pm$ SD; ***$P < 0.001$.

3.2. Lactate consumption and cascade catalytic ROS "storm" generation

Then the catalytic performance of LOX was evaluated by incubation with lactate. As depicted in Fig. 2F, the concentration of lactate in CeMOF group remained unchanged, but reduced 90.0% and 94.9% in LOX and LCeMOF groups, respectively. And the H_2O_2 production held lactate concentration-dependent manner in

LOX group (Fig. 2G). These results further indicated that LOX could effectively catalyze the oxidization of lactate into pyruvate and H_2O_2 for lactate exhaustion, and the CeMOF carrier effectively ensured the stability and catalytic activity of LOX[35]. Additionally, the catalytic behavior of CeMOF was further assessed. The CeMOF showed a mixed valence state with a Ce^{3+}/Ce^{4+} ratio of 5.83 (Fig. 2H), which was conducive to its oxidase-like activity[36]. The 2,2′-azinobis-(3-ethylbenzthiazoline-6-

sulfonic acid) (ABTS) could be converted into ABTS$^{\cdot+}$ in the presence of hydroxyl radicals ($\cdot$OH)[37−39]. It was found that CeMOF catalyzed $\cdot$OH formation in the presence of H_2O_2 at pH 6 and exhibited CeMOF concentration and time-dependent features (Fig. 2I and Supporting Information Fig. S4). Considering the self-supplied H_2O_2 of LOX-catalyzed lactate oxidation, we moved on to assess the cascade catalytic performance of LCeMOF. As illustrated in Fig. 2J, there was no $\cdot$OH generation in CeMOF group. In contrast, LCeMOF group induced more $\cdot$OH generation as lactate concentration increased. These results substantiated the catalytic reactions among LOX and CeMOF resulted in a large amount of ROS (Fig. 2A). In addition, the GSH level in 4T1 breast cancer cells was assessed (Fig. 2K). Without lactate incubation, LCeMOF group had little effect on GSH level. However, when CB839 concentration was 4 μmol/L, the GSH levels of CB839 and CLCeMOF groups decreased to 35.4% and 22.3%, respectively, which could be due to the that CB839 as a glutaminase inhibitor cut off glutamine metabolism and further indirectly reduced GSH generation[40]. Therefore, it was plausible that CB839 would enhance ROS "storm" in LCeMOF catalytic system.

3.3. Cytotoxicity and immune response in vitro

Encouraged by the admirable catalytic activity of CLCeMOF, we moved on to investigate the ROS production in 4T1 cells by using DCFH-DA fluorescent probe. All 4T1 cellular experiments were conducted with lactate incubation. Fig. 3A shows cells after different treatments displayed green fluorescence of DCFH. Of note, CLCeMOF group generated the highest amount of ROS, which was consistent with the above results. Besides, the lactate consumption effect of CLCeMOF is confirmed in Fig. 3B, which was expected to program TME[41]. Next, the toxicity effect of nanoplatform in 4T1 cells was investigated (Fig. 3C). Of note, CLCeMOF exhibited a strong therapeutic effect with decreased cell viability of 16.7 ± 3.2% at 5 mmol/L of lactate, far lower than LCeMOF (43.2 ± 7.2%) and CeMOF group (80.5 ± 5.2%). It was reasonable that ROS "storm" induced by the catalysis among LOX, CeMOF and CB839 enhanced oxidation damage on cells. What's more, glutamine metabolism inhibition by CLCeMOF brought out a wide-ranging metabolic inhibition in tumor cells that lacked metabolic plasticity. In this sense, integrating glutamine metabolic starvation therapy with ROS "storm", the designed nanoplatform (CLCeMOF) aggravated the imbalance of metabolism and oxidative stress prior to the evolutionary adaption of tumor cells, which prevented cell proliferation in the cradle.

More evidence showed that ROS with immunomodulation properties could induce ICD[42−46]. Then calreticulin (CRT) and high-mobility group box 1 (HMGB1) as ICD biomarkers were detected. CLSM images showed CLCeMOF with ROS "storm" effect exhibited the highest CRT exposure (Fig. 3D), and showed 2.3-fold higher HMGB1 release than that of the control group (Fig. 3E). Generally, ICD would recruit and activate DCs for antigen recognition and presentation[47−49]. Next, a transwell system was carried out to assess the DCs maturation behavior (Supporting Information Fig. S5). From the flow cytometry results (Fig. 3F), the frequency of matured DCs in CLCeMOF group was 1.80-, 1.73-, and 1.43-times higher than those of CeMOF, CB839, and LCeMOF group, respectively, which further confirmed that the CLCeMOF could stimulate the immune system for immunotherapy. As was known to all, the positive feedback of immunotherapy was significantly limited by high levels of immunosuppressive cells such as M2-TAMs. Inspired by the metabolic intervention and oxidative

stress by CLCeMOF, it was desired to investigate its behavior on TAMs phenotype. Interestingly, the positive M2-TAMs labeled with CD206 in CeMOF, CB839, LCeMOF, and CLCeMOF groups reduced to 18.3%, 17.7%, 9.6% and 2.6%, respectively, along with the increase of positive antitumor M1-TAMs labeled with CD86 (Fig. 3G). Furthermore, increased IL-12 and reduced IL-10 secretion from TAMs were found in these groups (Fig. 3H). The TAM re-polarization behavior of CLCeMOF might be contributed to CB839 mediated "metabolic checkpoint" blockade in glutamine metabolism-dependent M2-TAMs, lactate exhaustion mediated cAMP-dependent signal pathway inhibition, as well as ROS mediated NF-κB activation. Hence, these results indicated that CLCeMOF intervened in both metabolite (lactate exhaustion) and metabolic pathway (glutamine antagonism), which was conducive to reprogramming immunosuppressive TME and restoring antitumor immunity for reinforced immunotherapy.

3.4. In vivo antitumor efficacy evaluation

Next, we explored the feasibility in 4T1 tumor-bearing mice. To reveal the *in vivo* behavior of CLCeMOF, the pharmacokinetic parameters of intravenously injected CLCeMOF were assessed by monitoring the contents of Ce in the blood of mice in the time courses. After fitting Ce concentrations in the blood to times based on a two-compartment model (Supporting Information Fig. S6), the distribution half-life ($t_{1/2\alpha}$) and elimination half-life ($t_{1/2\beta}$) of CLCeMOF were determined to be 1.20 ± 0.15 and 5.36 ± 0.66 h, respectively. The clearance rate of CLCeMOF was calculated to be 0.36 ± 0.05 mL/min, the value of area under the curve (AUC) was 303.06 ± 36.74 μg min/mL, and the mean residence time (MRT) was 4.98 ± 0.21 h. The above results demonstrated that CLCeMOF could circulate well in blood, which was of great significance for further exploration of its application in cancer treatment. The *in vivo* distribution of CLCeMOF was investigated in fluorescent imaging (Fig. 4A and Supporting Information Fig. S7). Compared with free IR783, CLCeMOF/IR783 accumulated significantly in the tumor site, showing an excellent tumor targeting ability due to enhanced permeability and retention effect. The enhanced green fluorescence of DCFH was visualized in CLCeMOF group (Fig. 4B), indicating the ROS "storm" generation. Compared with the saline group, both CB839 and CLCeMOF groups significantly reduced the cellular glutaminase level, which would block cellular glutamine metabolism (Fig. 4C and D). The lactate exhaustion effect of CLCeMOF was also confirmed in the tumor site (Fig. 4E), which was consistent with *in vitro* results. These results are anticipated to improve the therapeutic effect of the metabolic intervention. Next, the antitumor efficacy of CLCeMOF was evaluated (Fig. 4F). Fig. 4G shows that LCeMOF induced a limited inhibition of tumor growth. Of note, CLCeMOF group displayed the highest tumor growth inhibition, and 22.2% of mice realized complete tumor regression. The digital photographs of tumors and tumor weights after the death of mice or at the end of the experiment were shown in Supporting Information Figs. S8 and S9. Without abnormalities in body weight and various organs (Fig. 4I and Supporting Information Fig. S10), CLCeMOF extended the survival rate of mice to 77.8% (Fig. 4H). By contrast, none of the saline groups survived on Day 22. What's more, the pathological analysis revealed the CLCeMOF treatment brought out a large amount of apoptosis and CRT exposure (Fig. 4J and K), indicating an ICD-induction efficacy. Therefore, the excellent therapeutic effect of CLCeMOF showed its reinforced immunotherapy to break the evolutionary adaptability of the tumor.
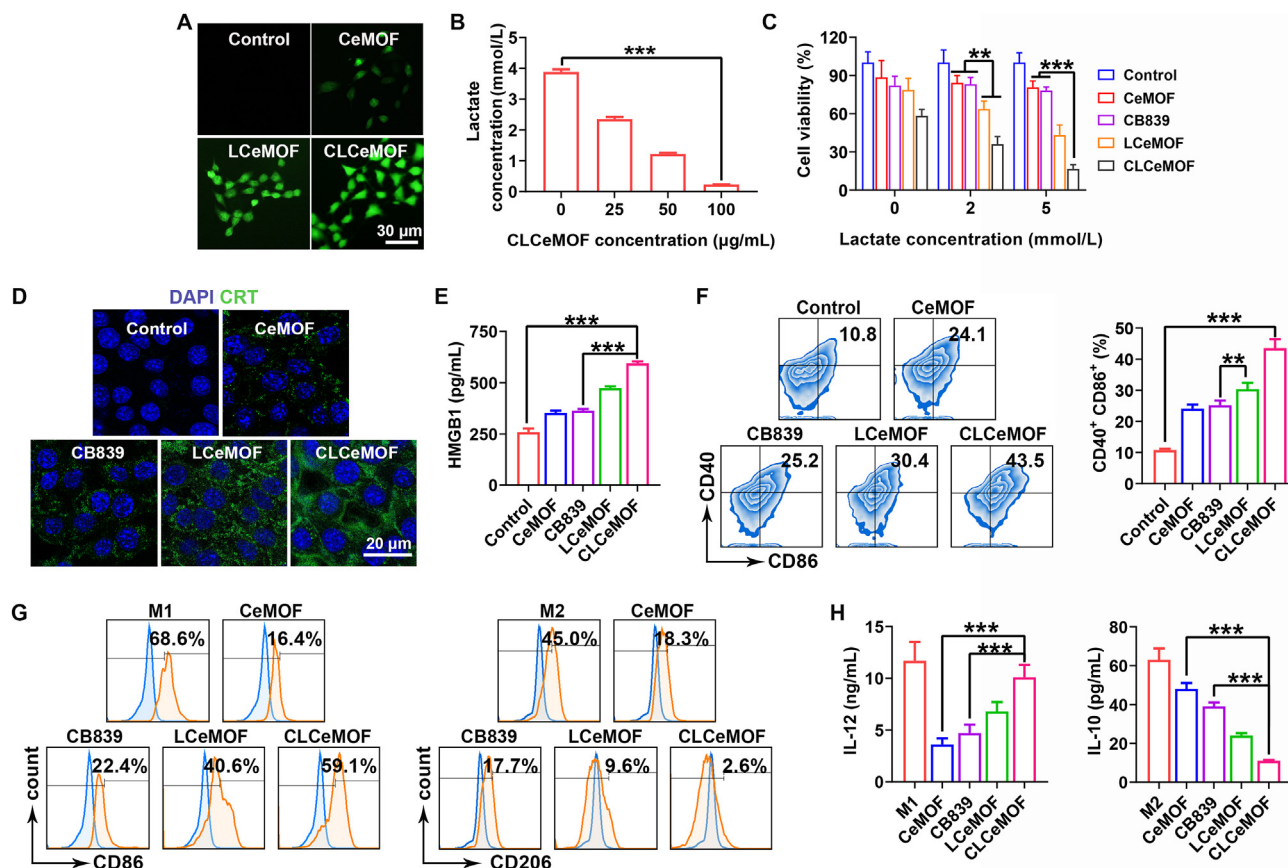
Figure 3 Cytotoxicity and immune response *in vitro*. (A) ROS detection in 4T1 cells (scale bar = 30 μm). (B) lactate consumption effect of CLCeMOF in 4T1 cells ($n = 3$). (C) Cell viability of 4T1 cells ($n = 6$). (D) CRT exposure (scale bar = 20 μm). (E) Released HMGB1 detection ($n = 3$). (F) Flow cytometric plot of DC maturation (CD40+CD86+) ($n = 3$). (G) Flow cytometric assay of the expression of CD86 and CD206 on the surface of TAMs (H) ELISA assay of IL-12 and IL-10 in TAMs ($n = 3$). Data are presented as mean ± SD; **$P < 0.01$, ***$P < 0.001$.

3.5. Immune cells infiltration and immune memory responses investigation

To evaluate the various cells mobilization effect in immunometabolic therapy, the infiltration of the immune cells into tumor was investigated. On basis of the TAM re-polarization behavior *in vitro*, the phenotype of TAMs in tumor was detected and the results are shown in Supporting Information Fig. S11. In comparison with the saline group, all CeMOF, LCeMOF and CLCeMOF groups showed an increased expression of M1 TAMs markers (TNF-α and iNOS) as well as a reduced expression of M2 TAMs marker (arginase 1). Additionally, the flow cytometry analysis also demonstrated the M1 repolarization (Fig. 5A and B). What's more, flow cytometry was used to investigate the abundance of infiltrating immune cells, and representative gating strategies for lymphocytes in tumors are shown in Supporting Information Fig. S12. The flow cytometric results demonstrated that the abundance of other lymphocytes in tumor site and tumor-draining lymph nodes altered, such as the increased CD8+ T lymphocytes and DCs, as well as the decreased glutamine-dependent MDSCs and Tregs (Fig. 5C–E, Supporting Information Figs. S13 and S14). And similar results are also validated in immunofluorescence images (Supporting Information Fig. S15). In detail, CD8+ T lymphocytes in CeMOF, CB839, LCeMOF and CLCeMOF groups were 1.5-, 1.9-, 2.1- and 2.3-fold higher than that of the saline group, respectively (Fig. 5C). Some reports indicated that the differentiation or behavior of CD8+ T

lymphocytes with adaptive metabolic reprogramming ability might alter after metabolic intervention[32,50]. Herein, the function of CD8+ T lymphocytes was assessed. Interestingly, the increased activation marker CD69 and anti-apoptotic protein MCL-1 were recorded after CB839 treatment (Supporting Information Figs. S16 and S17). And the flow cytometry analysis in Fig. 5F shows CB839 and CLCeMOF increased the frequency of effector memory T lymphocytes, ~2.4- and 4.4-times higher than the saline group. Therefore, these results suggest the glutamine antagonism of CB839 could reprogram CD8+ T lymphocytes toward a highly activated, long-lived and memory-like phenotype (CD8+ Thigh lymphocytes), which might be due to the up-regulation of acetate metabolism[32]. Fig. 5G reveals that the serum concentrations of antitumor cytokines (IL-6, IL-12, IFN-γ, TNF-α) significantly increased. Therefore, harnessing the metabolic differences to inhibit glutamine metabolism reduced tumor and immunosuppressive cells while enhancing the activity of positive immunoregulatory cells. In addition, the exhaustion of immunosuppressive lactate also repolarized immunosuppressive TME toward one supporting antitumor immunity. In this sense, the CLCeMOF intervened both metabolite (lactate) and cellular metabolic pathways, which altered overall cell fates toward their optimal immunity state.

Inspired by the memory-like property of CD8+ T lymphocytes, the immune memory responses against tumor relapse were investigated by i.v. injection of 4T1-luc cells. The results in Fig. 5H and I shows that CLCeMOF group displayed much
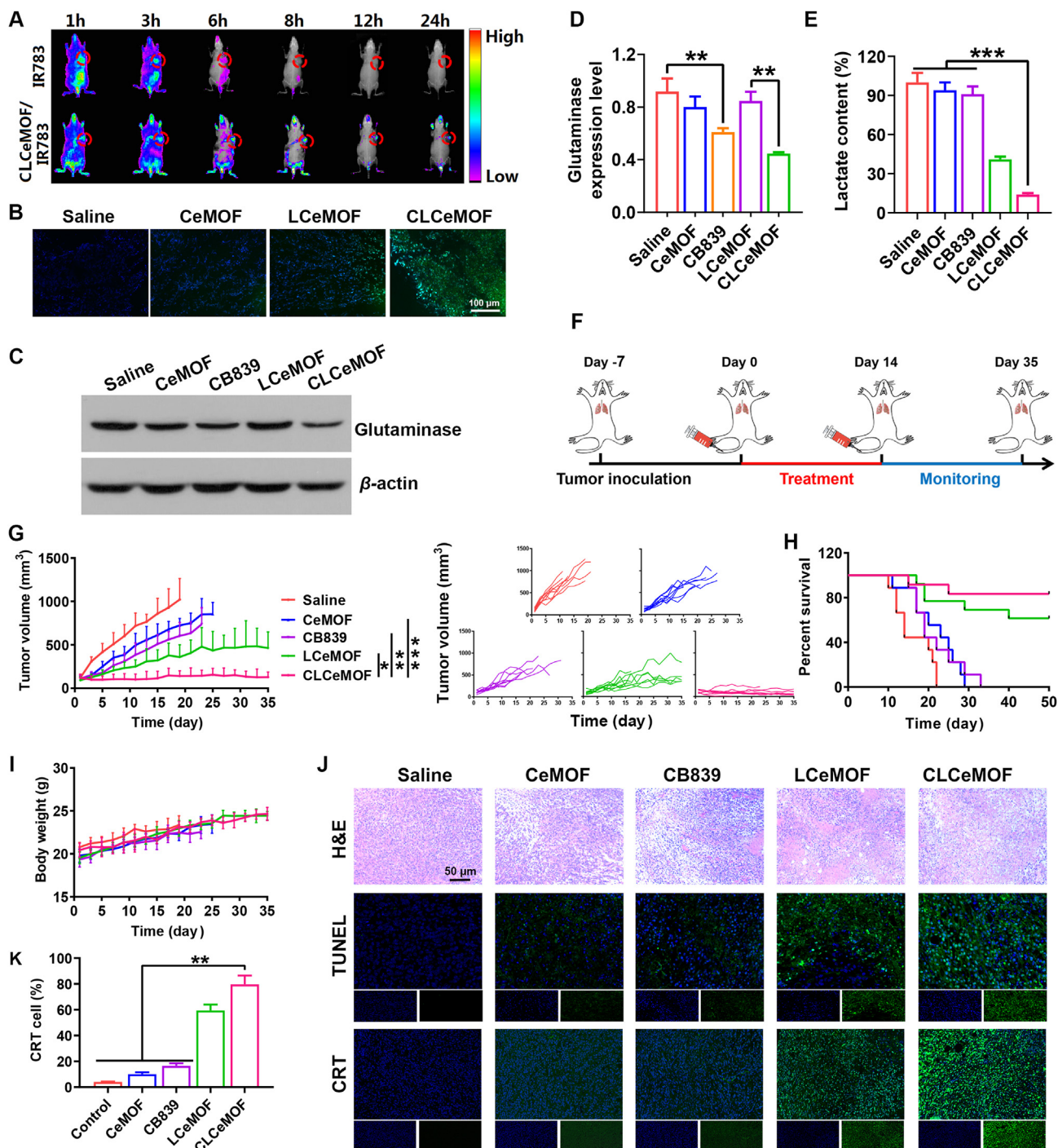
Figure 4 *In vivo* antitumor efficacy evaluation. (A) Fluorescent imaging of 4T1 tumor-bearing mice marked the tumor site with a red circle (B) Fluorescence images of the frozen tumor to observe ROS generation by DCFH-DA staining (scale bar $= 100$ μm). (C) Western blotting analysis of glutaminase (D) Quantified results of glutaminase from Western blot results ($n = 3$). (E) Intratumoral lactate levels detection ($n = 3$). (F) Treatment schedule (G) Tumor volume curves ($n = 9$). (H) Survival rate ($n = 9$). (I) Body weight changes ($n = 9$). (J) H&E, TUNEL and CRT staining of tumors (scale bar $= 50$ μm). (K) Quantitative analysis of CRT-positive cells in (J). Data are presented as mean $\pm$ SD; $*P < 0.05$, $**P < 0.01$, $***P < 0.001$.

cleaner lungs in comparison with the saline group, significantly suppressing 93.2% of lung metastasis. H&E staining images suggest a consistent tendency (Fig. 5H). The above results imply the potential of CLCeMOF for long-term antitumor relapse capability and metastasis prevention.

3.6. Metabolic and transcriptomic analysis

Encouraged by the overall cell mobilization effect of the metabolic intervention strategy, we moved on to explore the metabolism mechanism *in vivo* by metabolomics in mice after
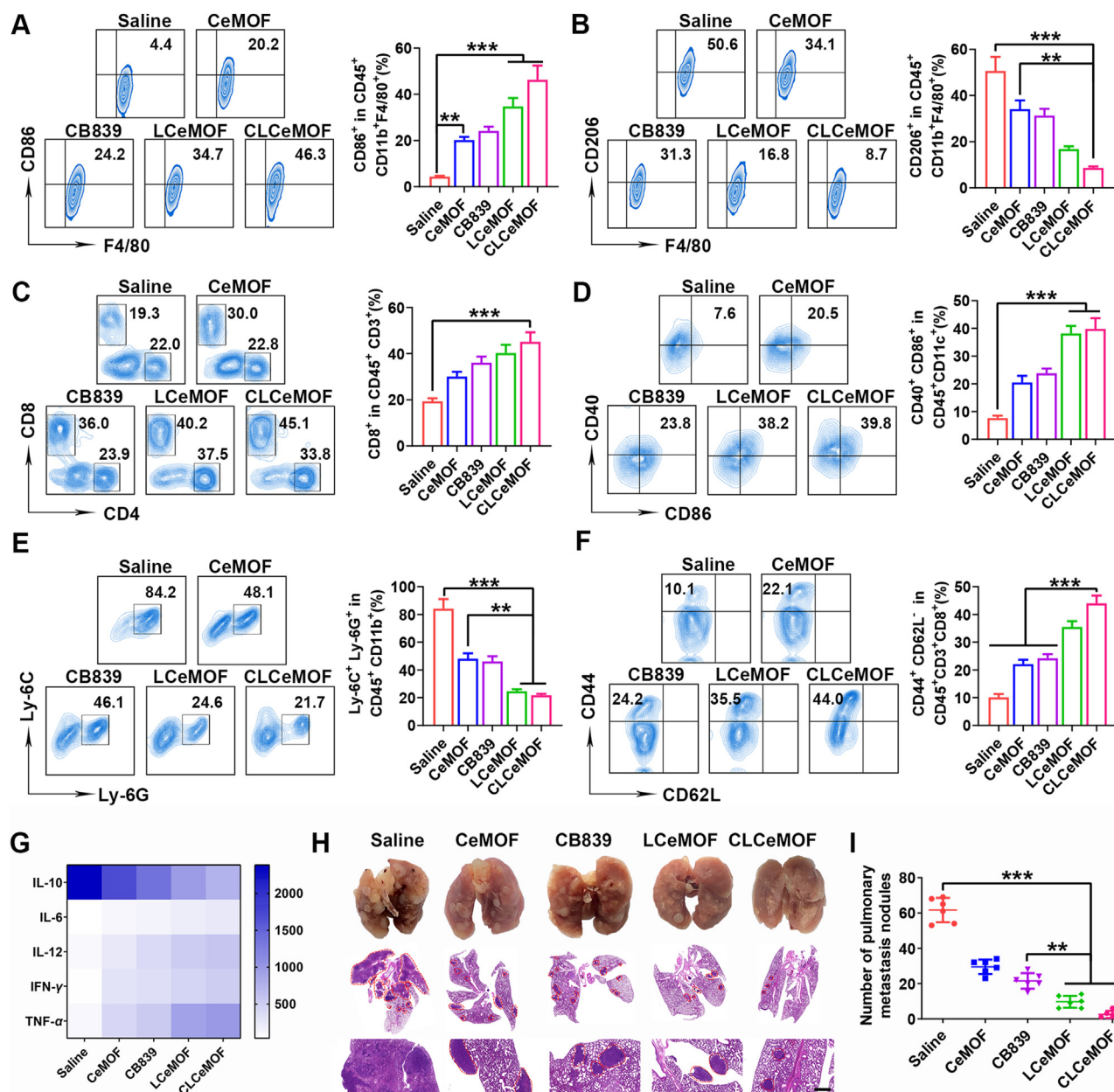
Figure 5 Immune cell infiltration and immune memory responses investigation. Flow cytometry plots and proportions of M1-TAMs (CD45$^+$CD11b$^+$F4/80$^+$CD86$^+$ cells) (A), M2-TAMs (CD45$^+$CD11b$^+$F4/80$^+$CD206$^+$ cells) (B), CD8$^+$ T lymphocytes (CD45$^+$CD3$^+$CD8$^+$) (C), DCs (CD45$^+$CD11c$^+$CD40$^+$CD86$^+$ cells) (D) and MDSCs (CD45$^+$CD11b$^+$Ly-6C$^+$Ly-6G$^+$ cells) (E) in tumors ($n = 3$). (F) Flow cytometry plots and proportions of memory-like CD8$^+$ T cells (CD45$^+$CD3$^+$CD8$^+$CD44$^+$CD62L$^-$) in spleen ($n = 3$). (G) The cytokines level (pg/mL) in serum ($n = 3$). (H) Photographs and H&E staining of lungs on the last day of treatments (scale bar = 500 μm). A red circle marked the metastatic tumors in the lung. (I) Lung metastasis nodule counting ($n = 6$). Data are presented as mean ± SD; **$P < 0.01$, ***$P < 0.001$.

treatments. Endogenous metabolites were analyzed by UPLC–MS/MS and the metabolites in CLCeMOF group showed significantly different from those in the saline group. Pathway analysis results in Fig. 6A show that the most altered metabolites were mainly involved in glutamine, glutamate, GSH and some amino acid metabolism related to the tricarboxylic acid (TCA) cycle. As shown in Fig. 6C, after CLCeMOF treatment, glutamine levels increased, whereas malate and 2-hydroxyglutarate levels reduced in CLCeMOF group. These results show that CB839 as a glutaminase inhibitor cut off glutamine metabolism, and caused less

conversion of glutamine to glutamate, which reduced TCA cycle intermediates. Metabolite set enrichment analysis of upregulated and downregulated metabolites displayed the enrichments in "ammonia recycling", "mitochondrial electron transport chain", "malate-aspartate shuttle", "urea cycle", "glycine and serine metabolism", "aspartate metabolism", "amino sugar metabolism", etc (Fig. 6B). The above results reveal that CLCeMOF mediated glutamine metabolism blocking could not only intervene GSH level and further redox balance but also disrupted anaplerotic flux of glutamine into TCA cycle and further energy production in the
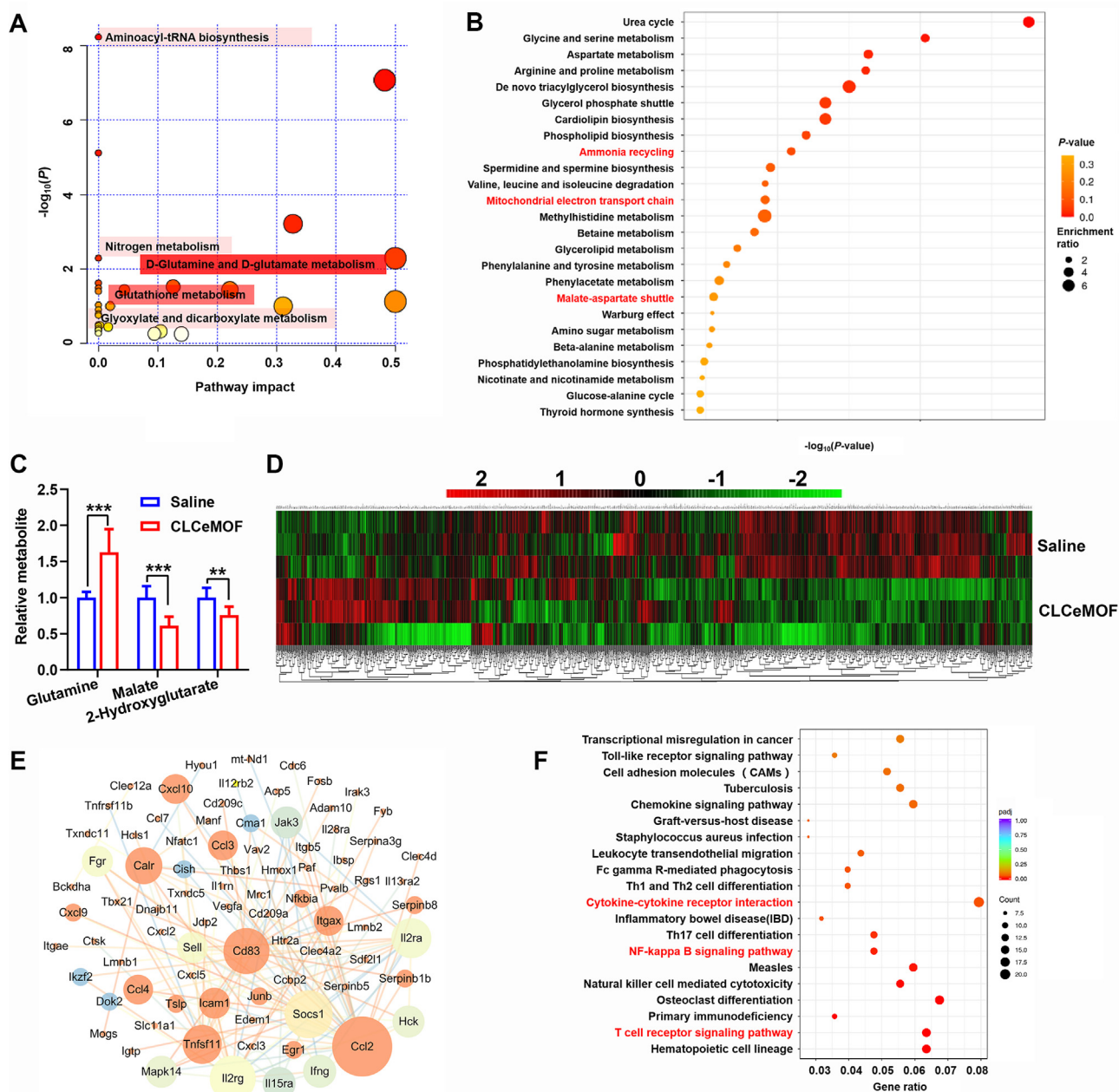
Figure 6 Metabolic and transcriptomic analysis. Pathway analysis (A) and enrichment analysis (B) of significant differential metabolites (CLCeMOF *vs.* saline). (C) Relative metabolite abundances in saline and CLCeMOF groups (D) Differentially expressed genes of the tumors were screened from saline and CLCeMOF group. (E) Functional association networks of the immune-related genes (CLCeMOF *vs.* saline). (F) KEGG enrichment analysis for studying the pathways of immunity activation (CLCeMOF *vs.* saline). Data are presented as mean ± SD (n = 3); **$P < 0.01$, ***$P < 0.001$.

tumor as a whole. To understand the changes from metabolomics, we performed transcriptomic analysis to investigate the immune state in the tumor site. A total of 25,102 genes of tumors were screened (Fig. 6D), and the genes in CLCeMOF group were well isolated and possessed biological repeatability in comparison with saline groups (adjusted $P<0.05$ and FC>1.5). Results in Supporting Information Fig. S18 show that 624 and 480 transcripts were, respectively, upregulated and downregulated in CLCeMOF group relative to the saline group, indicating the transcriptional-level change. And functional gene networks showed most of the upregulated genes (*Ccl2*, *Cd83*, *Tnfsf11*, etc.) corresponded to

immune responses (Fig. 6E). These results imply that the glutamine metabolism inhibition and immunosuppressive lactate exhaustion could effectively reprogram various cells toward their optimal immunity state. Interestingly, the kyoto encyclopedia of genes and genomes (KEGG) pathway analysis showed that 20 pathways with differentially expressed genes were enriched (Fig. 6F), suggesting that CLCeMOF mediated immune responses were dependent on "cytokine−cytokine receptor interaction", "NF-κB signaling pathway", "T cell receptor signaling pathway", "Toll-like receptor signaling pathway", etc. In this sense, it was reasonable that CLCeMOF with metabolic intervention could alter

the functions and behaviors of cells, even the gene expression, which was responsible for potent antitumor responses.

4. Conclusions

In summary, we developed a metabolic intervention strategy to break the evolutionary adaptability of tumors for reinforced immunotherapy. The CLCeMOF not only exhausted lactate to reprogram TME, but also inhibited glutamine metabolism from altering cell viability and differentiation. By intervening in both metabolite and cellular metabolic pathways, overall cell fates were improved toward the desired situation for immunotherapy. Notably, the $CD8^+$ T_{high} lymphocytes were responsible for potent antitumor responses. Collectively, this study verified the feasibility and promise of metabolic reprogramming. And future work will focus on the metabolic interdependence of immune and tumor cells. It is believed that metabolic intervention broadens the spectra of cancers for immunotherapy.

Acknowledgements

Author contributions

Qianhua Feng and Lei Wang designed the research. Yutong Hao and Shuaiqi Yang carried out the experiments and performed data analysis. Xiaomin Yuan, Jing Chen, Yuying Mei and Lanlan Liu participated part of the experiments. Qianhua Feng and Lei Wang provided experimental drugs and quality control. Qianhua Feng wrote the manuscript. Junbiao Chang and Zhenzhong Zhang revised the manuscript. All of the authors have read and approved the final manuscript.

Conflicts of interest

The authors have no conflicts of interest to declare.

Appendix A. Supporting information

Supporting data to this article can be found online at https://doi.org/10.1016/j.apsb.2022.10.021.

References

1. Zhen WY, Liu Y, Wang W, Zhang MC, Hu WX, Jia XD, et al. Specific "unlocking" of a nanozyme-based butterfly effect to break the evolutionary fitness of thaotic tumors. *Angew Chem, Int Ed* 2020;**59**:9491−7.
2. Leone RD, Powell JD. Metabolism of immune cells in cancer. *Nat Rev Cancer* 2020;**20**:516−31.
3. Renner K, Singer K, Koehl GE, Geissler EK, Peter K, Siska PJ, et al. Metabolic hallmarks of tumor and immune cells in the tumor microenvironment. *Front Immunol* 2017;**8**:248.
4. Kedia-Mehta N, Finlay DK. Competition for nutrients and its role in controlling immune responses. *Nat Commun* 2019;**10**:2123.
5. Li XY, Wenes M, Romero P, Huang SCC, Fendt SM, Ho PC. Navigating metabolic pathways to enhance antitumour immunity and immunotherapy. *Nat Rev Clin Oncol* 2019;**16**:425−41.
6. Wegiel B, Vuerich M, Daneshmandi S, Seth P. Metabolic switch in the tumor microenvironment determines immune responses to anti-cancer therapy. *Front Oncol* 2018;**8**:284.
7. Shen LJ, Zhou TJ, Fan YT, Chang X, Wang Y, Sun JG, et al. Recent progress in tumor photodynamic immunotherapy. *Chin Chem Lett* 2020;**31**:1709−16.
8. Zhang ZZ, Wang QX, Liu Q, Zheng YD, Zheng CX, Yi KK, et al. Dual-locking nanoparticles disrupt the PD-1/PD-L1 pathway for efficient cancer immunotherapy. *Adv Mater* 2019;**31**:1905751.
9. Feng QH, Li YZ, Wang N, Hao YT, Chang JB, Wang ZY, et al. A biomimetic nanogenerator of reactive nitrogen species based on battlefield transfer strategy for enhanced immunotherapy. *Small* 2020;**16**:2002138.
10. Kaymak I, Williams KS, Cantor JR, Jones RG. Immunometabolic interplay in the tumor microenvironment. *Cancer Cell* 2021;**39**:28−37.
11. Kolb D, Kolishetti N, Surnar B, Sarkar S, Guin S, Shah AS, et al. Metabolic modulation of the tumor microenvironment leads to multiple checkpoint inhibition and immune cell infiltration. *ACS Nano* 2020;**14**:11055−66.
12. Brisson L, Banski P, Sboarina M, Dethier C, Danhier P, Fontenille MJ, et al. Lactate dehydrogenase B controls lysosome activity and autophagy in cancer. *Cancer Cell* 2016;**30**:418−31.
13. Daw CC, Ramachandran K, Enslow BT, Maity S, Bursic B, Novello MJ, et al. Lactate elicits ER-mitochondrial Mg^{2+} dynamics to integrate cellular metabolism. *Cell* 2020;**183**:474−89.
14. Zhou X, Zhao W, Wang MX, Zhang S, Li YH, Hu WX, et al. Dual-modal therapeutic role of the lactate oxidase-embedded hierarchical porous zeolitic imidazolate framework as a nanocatalyst for effective tumor suppression. *ACS Appl Mater Interfaces* 2020;**12**:32278−88.
15. Zhou Y, Tong F, Wl Gu, Sq He, Xt Yang, Jm Li, et al. Co-delivery of photosensitizer and diclofenac through sequentially responsive bilirubin nanocarriers for combating hypoxic tumors. *Acta Pharm Sin B* 2022;**12**:1416−31.
16. Gao F, Tang Y, Liu WL, Zou MZ, Huang C, Liu CJ, et al. Intra-/extracellular lactic acid exhaustion for synergistic metabolic therapy and immunotherapy of tumors. *Adv Mater* 2019;**31**:1904639.
17. Tang J, Meka AK, Theivendran S, Wang Y, Yang YN, Song H, et al. Openwork@Dendritic mesoporous silica nanoparticles for lactate depletion and tumor microenvironment regulation. *Angew Chem, Int Ed* 2020;**59**:22054−62.
18. Cao FF, Zhang Y, Sun YH, Wang ZZ, Zhang L, Huang YY, et al. Ultrasmall nanozymes isolated within porous carbonaceous frameworks for synergistic cancer therapy: enhanced oxidative damage and reduced energy supply. *Chem Mater* 2018;**30**:7831−9.
19. Wu XP, Gagliardi L, Truhlar DG. Cerium metal-organic framework for photocatalysisl. *J Am Chem Soc* 2018;**140**:7904−12.
20. Zhang S, Pei X, Gao HL, Chen S, Wang J. Metal-organic framework-based nanomaterials for biomedical applications. *Chin Chem Lett* 2020;**31**:1060−70.
21. Dang GH, Tran YBN, Pham TV, Pham VT, Luu NTH, Nguyen HD, et al. A cerium-containing metal-organic framework: synthesis and heterogeneous catalytic activity toward fenton-like reactions. *Chempluschem* 2019;**84**:1046−51.
22. Wang DD, Jana D, Zhao YL. Metal-organic framework derived nanozymes in biomedicine. *Acc Chem Res* 2020;**53**:1389−400.
23. Ren E, Pang X, Lei Z, Liu G. Vesicular antibodies for immunotherapy: the blooming intersection of nanotechnology and biotechnology. *Nano Today* 2020;**34**:100896.
24. Deng HZ, Yang WJ, Zhou ZJ, Tian R, Lin LS, Ma Y, et al. Targeted scavenging of extracellular ROS relieves suppressive immunogenic cell death. *Nat Commun* 2020;**11**:4951.

25. Bockamp E, Rosigkeit S, Siegl D, Schuppan D. Nano-enhanced cancer immunotherapy: immunology encounters nanotechnology. *Cells* 2020; **9**:2102.

26. Faubert B, Solmonson A, DeBerardinis RJ. Metabolic reprogramming and cancer progression. *Science* 2020;**368**:5473.

27. Sun XY, Wang MZ, Wang MS, Yu XT, Guo JY, Sun T, et al. Metabolic reprogramming in triple-negative breast cancer. *Front Oncol* 2020;**10**: 428.

28. O'Neill LAJ. A Broken krebs cycle in macrophages. *Immunity* 2015; **42**:393−4.

29. Gross MI, Demo SD, Dennison JB, Chen LJ, Chernov-Rogan T, Goyal B, et al. Antitumor activity of the glutaminase inhibitor CB-839 in triple-negative breast cancer. *Mol Cancer Therapeut* 2014;**13**: 890−901.

30. Boysen G, Jamshidi-Parsian A, Davis MA, Siegel ER, Simecka CM, Kore RA, et al. Glutaminase inhibitor CB-839 increases radiation sensitivity of lung tumor cells and human lung tumor xenografts in mice. *Int J Radiat Biol* 2019;**95**:436−42.

31. Ananieva E. Targeting amino acid metabolism in cancer growth and antitumor immune response. *World J Biol Chem* 2015;**6**:281−9.

32. Leone RD, Zhao L, Englert JM, Sun IM, Oh MH, Sun IH, et al. Glutamine blockade induces divergent metabolic programs to overcome tumor immune evasion. *Science* 2019;**366**:1013−21.

33. Jiang HM, Yin GX, Gan YB, Yu T, Zhang YY, Li HT, et al. A multisite-binding fluorescent probe for simultaneous monitoring of mitochondrial homocysteine, cysteine and glutathione in live cells and zebrafish. *Chin Chem Lett* 2022;**33**:1609−12.

34. Dai YJ, Ding YM, Li LN. Nanozymes for regulation of reactive oxygen species and disease therapy. *Chin Chem Lett* 2021;**32**: 2715−28.

35. Liao ZX, Fa YC, Kempson IM, Tseng SJ. Repolarization of M2 to M1 macrophages triggered by lactate oxidase released from methylcellulose hydrogel. *Bioconjugate Chem* 2019;**30**:2697−702.

36. Wang Y, Liang RP, Qiu JD. Nanoceria-templated metal organic frameworks with oxidase-mimicking activity boosted by hexavalent chromium. *Anal Chem* 2020;**92**:2339−46.

37. Heckert EG, Seal S, Self WT. Fenton-like reaction catalyzed by the rare earth inner transition metal cerium. *Environ Sci Technol* 2008;**42**: 5014−9.

38. Tang GH, He JY, Liu JW, Yan XY, Fan KL. Nanozyme for tumor therapy: surface modification matters. *Explorations* 2021;**1**:75−89.

39. Lee JY, Liao HW, Wang QY, Han J, Han JH, Shin HE, et al. Exploration of nanozymes in viral diagnosis and therapy. *Explorations* 2022; **1**:20210086.

40. Altman BJ, Stine ZE, Dang CV. From krebs to clinic: glutamine metabolism to cancer therapy. *Nat Rev Cancer* 2016;**16**:619−34.

41. Baltazar F, Afonso J, Costa M, Granja S. Lactate beyond a waste metabolite: metabolic affairs and signaling in malignancy. *Front Oncol* 2020;**10**:231.

42. Deng HZ, Zhou ZJ, Yang WJ, Lin LS, Wang S, Niu G, et al. Endoplasmic reticulum targeting to amplify immunogenic cell death for cancer immunotherapy. *Nano Lett* 2020;**20**:1928−33.

43. Li JJ, Anraku Y, Kataoka K. Self-boosting catalytic nanoreactors integrated with triggerable crosslinking membrane networks for initiation of immunogenic cell death by pyroptosis. *Angew Chem Int Ed Engl* 2020;**59**:13526−30.

44. Zhang W, Wang F, Hu C, Zhou Y, Gao HL, Hu J. The progress and perspective of nanoparticle-enabled tumor metastasis treatment. *Acta Pharm Sin B* 2020;**10**:2037−53.

45. Jana D, Zhao YL. Strategies for enhancing cancer chemodynamic therapy performance. *Explorations* 2022;**2**:20210238.

46. Ding Yy, Wang Yx, Hu Qy. Recent advances in overcoming barriers to cell-based delivery systems for cancer immunotherapy. *Explorations* 2022;**2**:20210106.

47. Yang Qc, Ma Xb, Xiao Y, Zhang T, Yang Ll, Yang Sc, et al. Engineering prodrug nanomicelles as pyroptosis inducer for codelivery of PI3K/mTOR and CDK inhibitors to enhance antitumor immunity. *Acta Pharm Sin B* 2022;**12**:3139−55.

48. He J, Huo Y, Zhang ZK, Luo YQ, Liu XL, Chen QY, et al. Generation of α Gal-enhanced bifunctional tumor vaccine. *Acta Pharm Sin B* 2022;**12**:3177−86.

49. Zhou FY, Feng B, Wang TT, Wang DG, Cui ZR, Wang SL, et al. Theranostic prodrug vesicles for reactive oxygen species-triggered ultrafast drug release and local-regional therapy of metastatic triple-negative breast cancer. *Adv Funct Mater* 2017;**27**:1703674.

50. Nabe S, Yamada T, Suzuki J, Toriyama K, Yasuoka T, Kuwahara M, et al. Reinforce the antitumor activity of CD8$^+$ T cells *via* glutamine restriction. *Cancer Sci* 2018;**109**:3737−50.